Spectrum Allocation for Non-Cooperative Radar Coexistence

Anthony F. Martone[1], *Senior Member*, *IEEE*, Kenneth I. Ranney[1], *Senior Member*, *IEEE*, Kelly D. Sherbondy[1], Kyle A. Gallagher[1], *Member*, *IEEE*, and Shannon Blunt[2], *Fellow*, *IEEE*
[1]U.S. Army Research Laboratory, 2800 Powder Mill Road, Adelphi, MD, USA
[2]University of Kansas – Radar Systems Lab, Lawrence, KS, USA

***Abstract*— Access to the electromagnetic spectrum is an ever-growing challenge for radar. Future radar will be required to mitigate RF interference from other RF sources, relocate to new frequency bands while maintaining quality of service, and share frequency bands with other RF systems. The spectrum sensing, multi-optimization (SS-MO) technique was recently investigated as a possible solution to these challenges. Prior results have indicated significant improvement in the signal-to-interference plus noise ratio (SINR) at the cost of a high computational complexity. However, the optimization computational cost must be manageable in real time to address the dynamically changing spectral environment. In this paper, a bio-inspired filtering technique is investigated to reduce the computational complexity of SS-MO. The proposed technique is analogous to the processing of the thalamus in the human brain in that the number of samples input to SS-MO is significantly decreased, thus resulting in a reduction in computational complexity. The performance and computational complexity of SS-MO and the proposed technique are investigated. Both techniques are used to process a variety of measured spectral data. The results indicate a significant decrease in computational complexity for the proposed approach while maintaining performance of the SS-MO technique.**

Keywords—radar, spectrum sharing, spectrum sensing, multi-objective optimization, waveform agility, dynamic spectrum access, cognitive radar

I. INTRODUCTION

Radar is facing an ever-growing challenge with regards to electromagnetic spectrum access [1]. One such challenge is radio frequency (RF) interference (RFI) that is caused by other RF sources in or near the band of the radar [2,3]. It has been shown that RFI significantly degrades performance for multiple radar types including air traffic control and weather [2]. The RFI challenge is exacerbated in the United States by the government's plan to make available 500 MHz of federal and nonfederal spectrum for mobile and fixed wireless broadband usage. Partitioning of this 500 MHz was first initiated in January 2015 by the Federal Communications Commission (FCC) in an auction of Advanced Wireless Service (AWS) licenses [4], with further auctions to follow. Government RF systems that operate in an auctioned band (or a future to-be-auctioned band) are required to relocate to new bands or share the band with commercial wireless devices. A related spectrum access challenge is minimization of RFI generated by the radar onto other RF systems, which is particularly problematic for ultra-wideband radars [5,6].

Future radars must have the capability to 1) mitigate RFI from other sources, 2) adaptively change frequency in real time while maintaining quality of service, and 3) minimize RFI to other RF systems. The research area of spectrum sharing has addressed many aspects of these spectrum challenges. Much of this research is focused on operation around 5 GHz [7], a potential band for future auction. Spectrum sharing is accomplished through cooperative policies or coexistence techniques by using time, frequency, polarization, and/or space-domain strategies [8].

Cooperative policies require that the radar communicates with other RF systems (e.g., a radio) through some form of common protocol [8]. Several cooperative policies have been proposed for radars, such as air traffic control, where sharing is accomplished through time-domain strategies [9,10]. This strategy essentially involves limiting the radio's operation when it is within the main beam of the radar. Bandwidth sharing is another cooperative policy where the bandwidth of interest is divided into multiple sub-bands and assigned to the radar and communication systems [11]. Other cooperative policies explore innovative radar waveform tailoring techniques to accommodate the transmissions of communication systems. For example, the work in [12,13] investigates time-varying spectral notches in the radar waveform to accommodate frequency-hopping communication systems. The technique in [14] projects a multiple input, multiple output (MIMO) radar signal onto the null space of the channel, thereby reducing interference to the communication system. Other tailoring techniques consider covert radar/communication applications (e.g., military applications) where the transmission signal is designed to propagate in a channel without being detected [15,16].

Coexistence techniques attempt to share the spectrum without the use of a common protocol by avoiding the interference radiated by in-band RF systems. The concept of coexistence has been explored extensively for radio and, more recently, for radar [17]. The goal of the radar is to dynamically access a particular spectral interval of bandwidth B, portions of which are being used by other RF systems. Ideally, the radar would use the entire bandwidth to achieve a fine range resolution. However, the radiation from other RF users generates RFI on the radar causing degradation in the signal-to-interference plus noise ratio (SINR). Coexistence, a two-step approach, first requires characterization of the electromagnetic environment (EME) via spectrum sensing followed by a technique to access the spectrum dynamically. Spectrum sensing detects the activity of other RF systems attempting to access the same band as the radar; well-known detection approaches include matched filtering, energy detection, and spectral correlation [18]. Using decision theoretic approaches, the radar then determines how to access the spectrum. Equal

sharing between multiple users, such as radar, cell phones, and WiFi, requires a simple and effective strategy to access the spectrum dynamically to share a frequency band of interest.

One coexistence strategy is to add spectral notches to the radar waveform [12,13,19-23]. These spectrally compliant waveforms have the capability to mitigate RFI to other RF emitters and maximize the available bandwidth. Approaches include interruption of the frequency-modulated continuous wave (FMCW) or step-frequency sweep [22], constrained optimization to tailor the waveform to meet design criteria [23], waveform pre-distortion [22], design and implementation of specialized waveforms and matched filter responses [20,21], and non-repeating FMCW methods to achieve low range sidelobes [12]. Several challenges exist with these approaches. One such challenge is the capability to achieve the null depth requirements for multiple wideband and narrowband nulls. For example, adding two nulls can degrade the null depth by 10 dB compared to the one null case [12]. In addition, realization of a nulled radiated waveform in hardware is limited and can result in further degradation of the null depth [13]. A challenge for the constrained optimization approach is computational complexity, which can be problematic for real-time adaptation to unknown, time-varying RF emitters. A final challenge is proper estimation of the null characteristics, e.g., how to optimally estimate the bandwidth of unknown RF emitters.

A possible solution to the notched waveform approach is selection of a single continuous sub-band for radar operation. This solution would simplify the waveform and hardware complexity of the aforementioned approaches at the tradeoff of a reduced bandwidth. However, when viewed from a radar resource management perspective, this bandwidth trade-off can be advantageous for particular modes of radar operation. For example, a search and track radar may not require maximum bandwidth when in search mode (i.e., simplify the waveform design and preserve as much SINR as possible); bandwidth can then be increased once the target is detected [24]. The continuous sub-band approach for radar coexistence was introduced in [25]. This technique, known as spectrum sensing multi-objective optimization (SS-MO), passively senses the EME to create an empirical estimate of interference via energy detection. Energy detection is advantageous since 1) it is efficiently implemented in hardware and 2) it does not require a priori knowledge of the RF systems operating in the desired spectrum of bandwidth B and is therefore capable of identifying RFI from several sources. This interference estimate is employed to form an SINR objective function via the radar range equation. Multi-objective optimization is then used to determine the sub-band that maximizes SINR and the available bandwidth in a joint manner. Note that maximizing the SINR objective function avoids sub-bands containing radiated emissions and inherently reduces the risk of interfering with other RF systems.

In [25, 26] the SS-MO technique was investigated for chirp and stepped-frequency waveform types, with significant SINR (25 dB) and peak-to-average sidelobe level (15 dB) improvements demonstrated. SS-MO provides an added resource to radar electronic support and is applicable to multiple radar waveforms and applications. It should be noted that SS-MO can be extended to identify multiple disjoint sub-bands for radar operation in addition to single sub-band optimization, and is therefore complementary to the notched waveform approaches discussed previously [27].

The original investigations of SS-MO [25, 26] considered weighted sum multi-objective optimization (WSMO) to perform an exhaustive search of the solution space. The computational complexity of WSMO is O(N2), where N is the number of frequency domain samples that are processed. Implementation of WSMO is therefore inadequate for radar applications that require fast solutions for target detection and classification. The computational complexity of WSMO also results in an inaccurate estimate when the RFI changes at a rate faster than SS-MO converges. The computational complexity of the SS-MO technique must therefore be reduced. More recently in [28] the performance of WSMO was compared to a genetic algorithm, where the computational complexity was reduced by the genetic algorithm. The challenge for the genetic algorithm is that the number of summations needed to estimate the interference is still large. Furthermore, the genetic algorithm requires a random value for its initial condition that results in significant performance fluctuations.

In this paper, the fast WSMO (fWSMO) is introduced as an alternative to WSMO. fWSMO is based on a technique to refine information in the spectrum by grouping regions of low- and high-power interference [29]. The refinement technique in [29] can be used for any RF application (radio or radar) and was originally analyzed for proof-of-concept purposes by processing a single spectrum. However, this refinement technique does not consider the optimization criteria required for WSMO and maximum performance cannot be achieved. The fWSMO approach uses multi-objective optimization in conjunction with the refinement technique to achieve the mutual benefit of low complexity for an optimized solution. fWSMO extends the proof-of-concept analysis in [29] by using a comprehensive spectral training set to identify parameters to maximize performance (Section V).

fWSMO is a bio-inspired processing technique analogous to the processing of the thalamus in the human brain. The thalamus regulates sensory input (excluding olfaction) from the external environment to reduce the amount of information sent to the cerebral cortex [30]. An abnormal thalamus disrupts the flow of information to the cerebral cortex, thereby overwhelming a person with external stimuli [31], a condition commonly observed in schizophrenia patients [31, 32]. In a similar way, the fWSMO approach reduces the number of samples input to WSMO, thus resulting in a significant reduction of computational complexity. The proposed technique is discussed and formulated in Section III, following an overview of the WSMO technique in Section II. Section IV introduces synthetic and measured spectral datasets used to train and test the algorithms. Section V uses the training dataset to identify the key parameters of fWSMO, followed by evaluation of both techniques in Section VI.

II. Spectrum Sensing for Radar

This section provides an overview of the general SS-MO approach followed by a detailed discussion of the WSMO technique. The fWSMO approach (Section III) refines the data prior to the exhaustive search process of WSMO. The formulation of WSMO was originally described in [25] and is summarized in this section for completeness.

A block diagram of the SS-MO technique is illustrated in Fig. 1. The overall goal of SS-MO is to identify an optimal sub-band, within an overall bandwidth, to maximize SINR and the usable bandwidth. Multiple ways of defining the sub-bands must therefore be examined. Spectrum sensing is first implemented to passively monitor the radar operating band B. The spectrum sensing receiver digitizes and processes the observed RF spectrum to generate a power spectrum estimate $\Theta = |\Phi(\{x_1, \ldots, x_N\})|^2 = \{\theta_1, \ldots, \theta_N\}$ of size N for frequencies $F = \{f_1, \ldots, f_N\}$, where θ_n is the n^{th} frequency domain sample, and $\Phi(\bullet)$ denotes the Fourier transform of the sequence. N time-domain samples $\{x_1, \ldots, x_N\}$ are processed by $\Phi(\bullet)$, where x_n is the n^{th} time-domain sample. In this development, the time-domain samples are complex valued. The frequency resolution of the power spectrum is defined as Δ_r and remains constant so that the noise is fixed between each sensing cycle. Here, the frequency resolution used for both the radar and spectrum sensing receiver is identical. Note that it is possible for the spectrum sensing receiver to use the same RF front-end as the radar or a separate front-end. The specific system design would be dependent on the radar application and size, weight, and power (SWaP) limitations.

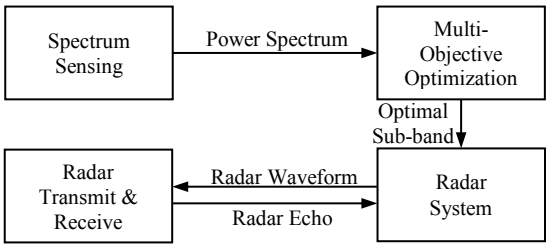

Fig. 1: SS-MO technique for radar.

After the spectrum sensing process is complete, the radar begins operation using the full bandwidth B (without knowledge of the RFI) until SS-MO converges to a solution. Radar performance should improve once the SS-MO solution is made available to the radar. The radar spectral footprint is also reduced thereby minimizing mutual interference. The radar then synthesizes the appropriate waveform using the optimal frequency allocation provided by SS-MO. The synthesized waveform is then transmitted at the start of the next coherent processing interval (CPI).

Multi-objective optimization is used to address two different objective functions. The SINR objective function is formed using the empirical estimate of the interference denoted as $\Gamma(\beta_i, f_j)$, where $\beta_i = i\Delta_r$ is the i^{th} sub-band bandwidth and $f_j \in F$ is the start frequency (the band edge) of this sub-band, for $i = \{1, \ldots, N\}$ and $j = \{1, \ldots, N - i + 1\}$. In total, there are $\overline{N} = (N^2 + N)/2$ possible sub-band combinations.

An example of how $\Gamma(\beta_i, f_j)$ is formulated is shown in Fig. 2 for $N = 5$ power spectrum estimate samples, or $\{\theta_1, \ldots, \theta_5\}$, with start frequencies $\{f_1, \ldots, f_5\}$ and $\overline{N} = 15$ available sub-bands. The bandwidth of each sub-band is shown on the right and the start frequency is shown above each bin. The finite number of possible combinations occur because each sub-band is formed by a contiguous set of frequencies. Each level in Fig. 2 corresponds to a particular sub-band size, and each element in a given level corresponds to a particular start frequency. The Level 1 elements (top row in Fig. 2) contain the power estimate values with a bandwidth equal to $\beta_1 = \Delta_r$ (i.e., the resolution of the power spectrum). Level 2 elements are formed by summing two sequential power estimate values from Level 1. The bandwidth of Level 2 is thus $\beta_2 = 2\Delta_r$ since two power estimate values are combined. Without loss of generality, the Level 5 element is formed by summing all five power estimate values such that the bandwidth is $\beta_5 = 5\Delta_r = B$.

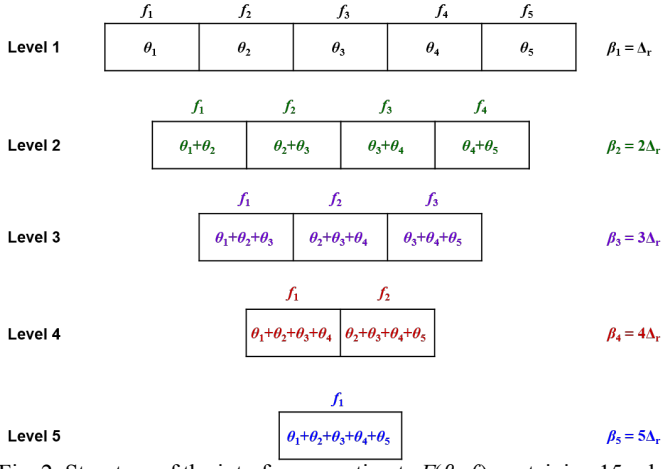

Fig. 2: Structure of the interference estimate $\Gamma(\beta_i, f_j)$ containing 15 sub-band combinations available for processing. The sub-band size increases as the samples are merged together. The start frequency is depicted above each cell.

The SINR objective function is formed next using the power spectrum and the receive power. The WSMO approach [25] uses the following recursive algorithm (exhaustive search) to process the power spectrum and form the empirical estimate of interference and noise:

$$\Gamma(\beta_i, f_j) = \begin{cases} \theta_j, & i = 1, j = 1, \ldots, N \\ \Gamma(\beta_1, f_j) + \Gamma(\beta_1, f_{1+j}) & i = 2, j = 1, \ldots, N\text{-}1 \\ \Gamma(\beta_{i-1}, f_j) + \Gamma(\beta_1, f_{i+j-1}) & i = 3, \ldots N, j = 1, \ldots, N\text{-}i\text{+}1 \end{cases} . \quad (1)$$

The receive power is modeled using the radar range equation and is defined as

$$P_r = P_t G^2 \lambda^2 \sigma N_P / [(4\pi)^3 R^4], \quad (2)$$

where P_t is the radar peak transmit power, G is the transmit and receive antenna gain, λ is the wavelength of the carrier frequency, N_P is the number of pulses within a CPI, R is the

arbitrary range to target, and σ is the target radar cross section (RCS).

The SINR objective function is then defined using (1) and (2):

$$Z_1(\beta_i, f_j) = P_r \tau \beta_i / \Gamma(\beta_i, f_j) = C \beta_i / \Gamma(\beta_i, f_j), \quad (3)$$

where τ is the radar pulse width and $C = P_r \tau$ is used to group together the generic parameters. The waveform type used by (3) supports a pulse compression waveform with a time-bandwidth (TB) product consistent with a contiguous bandwidth β_i; however, the SS-MO technique is modifiable to support multiple waveform types. The first objective of SS-MO is to adjust β_i and f_j to maximize (3).

The sub-band size is the second objective function and is defined as

$$Z_2(\beta) = \beta_i. \quad (4)$$

The second goal of SS-MO is to adjust β_i to maximize (4). Notice that the presence of β_i in both (3) and (4) establishes a fundamental conflict. To maximize (4), we require β_i to be as large as possible. However, since SINR greatly decreases for sub-bands containing RFI, this condition implies the more RFI is present as β_i increases and encompasses these RFI sub-bands, thereby decreasing SINR. Multi-objective optimization is used to maximize these conflicting objective functions by using the following linear weighting function [33]:

$$Z(\beta_i, f_j) = \alpha \acute{Z}_1(\beta_i, f_j) + (1-\alpha) \acute{Z}_2(\beta_i) \quad (5)$$

where $0 \le \alpha \le 1$ is a user-defined weighting parameter, $\acute{Z}_1(\beta_i, f_j) = Z_1(\beta_i, f_j) / \max[Z_1(\beta_i, f_j)]$ is the normalized objective function of $Z_1(\beta_i, f_j)$, and $\acute{Z}_2(\beta_i) = Z_2(\beta_i, f_j) / \max[Z_2(\beta_i, f_j)]$ is the normalized objective function of $Z_2(\beta_i)$. The weighting parameter α is selected to emphasize one objective function over the other and is dependent on the radar application. For example, it would be beneficial to set $\alpha \le 0.5$ for high spatial radar applications that require large bandwidths. The optimal solution $\{\beta_i^*, f_j^*\}$ to (5) is obtained via

$$\{\beta_i^*, f_j^*\} = \underset{(\beta_i, f_j)}{\operatorname{argmax}} [Z(\beta_i, f_j)], \quad (6)$$

subject to

$$Z_1(\beta_i, f_j) \ge Z_{1,\min} \quad (7)$$

and

$$Z_2(\beta_i, f_j) \ge Z_{2,\min}, \quad (8)$$

where $Z_{1,\min}$ is the minimum SINR required for detection and $Z_{2,\min}$ is the minimum bandwidth needed to meet range resolution requirements. The constraints of (7) and (8) require that (6) produces a feasible solution.

The computational complexity of the WSMO approach is summarized in the following list. The multi-objective optimization procedure requires a total of N^2 summations, $(3N^2 + 5N) / 2$ multiplications and divisions, and is $O(N^2)$.

a) Equation (1): The computational complexity needed to form (1) requires $(N^2 - N) / 2$ summations.
b) Equation (2): The receive power is updated every CPI. For example, the range to target R may increase or decrease over time. Only one multiplication is needed to compute (2) and is ignored since it does not impact computational complexity.
c) Equation (3): Since (3) is updated each CPI and β_i is size N, the numerator in (3) requires N multiplications (i.e., $P_r \tau \beta_i$). Subsequently, $(N^2 + N) / 2$ divisions by $\Gamma(\beta_i, f_j)$ are then needed to form (3). The total number of multiplications and divisions is $(N^2 + 3N) / 2$.
d) Equation (4): Since β_i is known *a priori* and does not change per CPI cycle, the formation of (4) does not contribute to the computational complexity.
e) Equation (5): The variable α is constant in this development and β_i is known *a priori*; therefore, $(1-\alpha) \acute{Z}_2(\beta_i, f_j)$ does not contribute to the computational complexity. The quantity $\alpha \acute{Z}_1(\beta_i, f_j)$ requires $(N^2 + N) / 2$ multiplications (multiplication by α), $(N^2 + N) / 2$ divisions (normalization of objective function), and $(N^2 + N) / 2$ summations (summation of the objective functions). The total number of multiplications and divisions is $(N^2 + N)$.

The SS-MO technique is implemented at the start of the CPI so that the radar has an up-to-date measure of the RFI. Ideally, the radar would then transmit N_P pulses for the remainder of the CPI; however, since the radar devotes resources to the implementation of the SS-MO technique, additional time is needed. For a radar system design requiring a fixed timeline (i.e., a constant CPI), this added processing time is compensated for by reducing the number of pulses on target, which consequently decreases SINR. Clearly, the computational complexity of the SS-MO technique should be at a minimum. The CPI time for radar operation in this context is defined as

$$T = T_C + T_{FFT} + T_{MO} + T_R, \quad (9)$$

where T_C is the time needed to collect the time-domain samples, T_{FFT} is the time needed to estimate the power spectrum via a fast Fourier transform (FFT), T_{MO} is the multi-objective optimization processing time, and T_R is the radar operation time. In this development, the times T_C, T_{FFT}, and T_R are constant and cannot be reduced. The computational complexity of the FFT and power spectrum is $O(N \log N)$, which is far less than the complexity of $O(N^2)$ needed for WSMO (i.e., $T_{FFT} < T_{MO}$). The collection time T_C varies based on the radar application. For example, the collection time needed to process $N = 1000$ time-domain samples at a rate of 200 mega samples per second is $T_C = 5$ μs (these parameter definitions are similar to those discussed in the experiments section, Section IV). The time T_{MO} varies greatly between radar applications since it depends on the digital hardware architecture, the processor speed, and the size, weight, power, and cost (SWaP-C) requirements. For radar applications where $T_{MO} \ge T_C$, and given that $T_{MO} > T_{FFT}$, T_{MO} should be reduced so that (9) is minimized.

The next section introduces the fWSMO approach, which reduces the computational complexity of WSMO, a result that would decrease T_{MO}.

III. Fast Weighted Sum Multi-Objective Optimization

A block diagram of the proposed fWSMO technique is shown in Fig. 3. An overview of the technique is presented here followed by a detailed description of the implementation in Sections IIIa and IIIb. The proposed technique is not a new optimization routine, but rather a method to refine spectral data input into any optimization method to make it fast (i.e., the "f" in fWSMO), with the refinement operations implemented in the first two blocks of Fig. 3. The refinement operations are based on the work described in [29], though the approach in [29] did not consider the optimum sub-band for radar operation. The fWSMO approach operates on the power spectrum estimate. An example power spectrum is shown in Fig. 4 for illustration purposes. This power spectrum was collected by a spectrum analyzer with B = 100 MHz and Δ_r = 0.1 MHz. The full details of this collection process are discussed in Section IV.

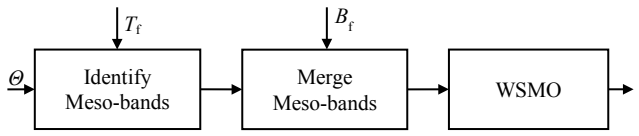

Fig. 3. Multi-objective optimization implemented using fWSMO.

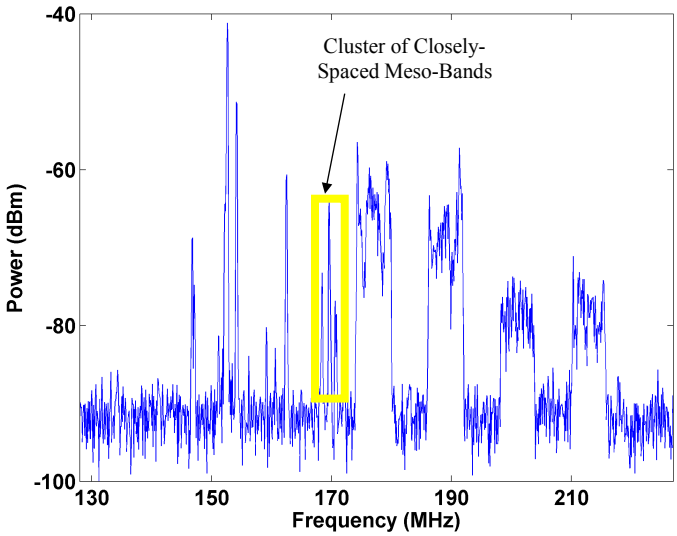

Fig. 4. Example measured power spectrum with B = 100 MHz and Δ_r = 0.1 MHz.

The fWSMO approach first identifies regions of low- and high-power interference, where each region corresponds to a "meso-band." The meso-bands constitute a new, refined power spectrum estimate and are used to replace the power spectrum estimate Θ as input to WSMO. Define the set of $K \le N$ meso-bands as $\Phi = \{\Phi_1, \ldots, \Phi_K\}$ and let $\Phi_k \in \Phi$. The meso-band Φ_k has an associated start position $\bar{S}_k \in \{1, \ldots, N\}$, end position $\bar{E}_k \in \{1, \ldots, N\}$, the number of frequency bins $\bar{l}_k \in \{1, \ldots, N\}$, and interference power

$$\bar{\Gamma}_k = \sum_{n=\bar{S}_k}^{\bar{E}_k} \theta_n. \tag{10}$$

The value Φ_k is deemed to be a "low-power meso-band" when $\theta_n < T_f$ for all $n \in \{\bar{S}_k, \ldots, \bar{E}_k\}$, where T_f is a user-defined threshold that is examined in Section V. Alternatively, Φ_k is deemed to be a "high-power meso-band" when $\theta_n \ge T_f$ for all $n \in \{\bar{S}_k, \ldots \bar{E}_k\}$. It should be noted that meso-bands are deemed either low- or high-power, never both, and alternate between low- and high-power. In other words, a low-power meso-band might be surrounded by high-power meso-bands, or a high-power meso-band could be surrounded by low-power meso-bands. The length is used to compute the bandwidth β_i. The computational complexity of this process is $O(N)$ due to the summations used to determine $\bar{\Gamma}_k$ and $\bar{l}_k$.

It is possible that the spectrum contains closely spaced narrowband interference resulting in a cluster of several meso-bands. Fig. 4 illustrates an example of such a cluster where 7 meso-bands exist within a 5 MHz bandwidth. If the number of meso-bands is large such that $K \approx N$, then the resulting computation complexity of WSMO would be $O(N^2)$. Since ideally $K << N$, the second step in fWSMO is to merge these closely spaced meso-bands. A merged meso-band is then considered high-power since it contains interference from the high-power meso-bands. The number of frequency bins corresponding to all the low-power meso-bands in Φ must therefore be examined to determine which would best support radar operation.

Let Φ_k correspond to a low-power meso-band. Then Φ_k is merged with Φ_{k-1} and Φ_{k+1} if $\bar{l}_k \le B_L$, where $B_L = B_f / \Delta_r$, and B_f is a user-defined nominal bandwidth corresponding to the required bandwidth of the low-power meso-bands. Define the set of $\hat{K} \le K$ merged meso-bands as $\hat{\Phi} = \{\hat{\Phi}_1, \ldots, \hat{\Phi}_{\hat{K}}\}$ with start position $\hat{S}_{\hat{k}} \in \{1, \ldots, K\}$, end position $\hat{E}_{\hat{k}} \in \{1, \ldots, K\}$, number of frequency bins $\hat{l}_{\hat{k}} = \bar{l}_{k-1} + \bar{l}_k + \bar{l}_{k+1}$, interference power $\hat{\Gamma}_{\hat{k}} = \sum_{l=-1}^{1} \bar{\Gamma}_{k+l}$, and $\hat{k} \in \{1, \ldots, \hat{K}\}$. Note that the process of merging the meso-bands is recursive, hence the index k-1 in the definition of $\hat{l}_{\hat{k}}$ and $\hat{\Gamma}_{\hat{k}}$, and is discussed in detail in Section III-B. Note also that $\hat{\Gamma}_{\hat{k}}$ is used to find the average power per meso-band and replaces θ_j in (1) for WSMO. The meso-band bandwidth is defined as $\hat{\beta}_{\hat{k}} = \hat{l}_{\hat{k}} \Delta_r$ with start frequency $f_{\hat{S}_{\hat{k}}}$. This merging process reduces the number of meso-bands to $\hat{K} \le K$. It should be noted that the merging process reduces the set of solutions found by WSMO, and it is therefore possible that the optimal solution is not reached. The computational complexity of this process is dependent on the summations used to find $\hat{\Gamma}_{\hat{k}}$ and $\hat{l}_{\hat{k}}$ and the multiplications used to find $\hat{\beta}_{\hat{k}}$, both of which are $O(K)$.

The algorithm flow-chart of Fig. 5 provides a high-level overview (qualitative) of the meso-band Identify and Merge functions of Fig. 3. The detailed functionality (quantitative) of the meso-band Identify and Merge processes are described in Sections III-A and III-B, respectively. The algorithm initializes

the first meso-band Φ_1 and the variables $k = 1$, $n = 1$. Each power sample is then compared to T_f. A low-power meso-band is indicated if $\theta_n < T_f$ and a high-power meso-band is indicated if $\theta_n \geq T_f$. An additional condition, $\theta_{n-1} < T_f$ or $\theta_{n-1} \geq T_f$, is used to determine whether θ_n should be added to an existing meso-band or if it should be the start of a new meso-band. If a new meso-band is indicated, then the current meso-band is finalized, the count incremented as $k = k + 1$, and the new meso-band parameters are initialized. Otherwise, the current meso-band parameters are updated. This process repeats until $n > N$.

The meso-band Merge algorithm (Fig. 5) initializes parameters ($\hat{l}_{\hat{k}}$, $\hat{T}_{\hat{k}}$, $\hat{S}_{\hat{k}}$, $\hat{E}_{\hat{k}}$) and variables $k = 1$ and $\hat{k} = 1$. This algorithm examines the bandwidth of low-power meso-bands. If the bandwidth of the low-power meso-band is small, then the condition $\bar{l}_k < B_L$ is true and the current meso-band (Φ_k) must be merged. The condition $\bar{l}_{k-2} < B_L$ examines if the prior meso-band (Φ_{k-2}) was merged, thereby indicating that a merge is in progress. If true, then the current meso-band is merged with the prior meso-band recursively; otherwise, a new merge is initialized. The variable $k = k + 2$ is then updated and the next low-power meso-band is examined. If the bandwidth of the low-power meso-band is large, then the condition $\bar{l}_k < B_L$ is false and no merge is required. If a merge was in progress (i.e. $\bar{l}_{k-2} < B_L$), then the merged meso-band is finalized as a new high-power meso-band. Otherwise, no merge is needed for the current low-power meso-band. This process repeats until $k > K$.

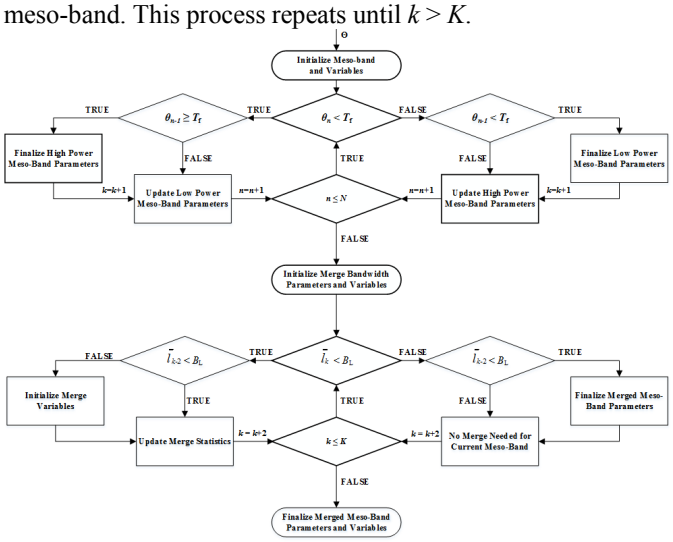

Fig. 5. Algorithm flow chart depicting a high-level overview of the Identify and Merge meso-bands functions.

The bandwidth and start frequency pairs $\{\hat{\beta}_{\hat{k}}, f_{\hat{S}_{\hat{k}}}\}$ of the merged meso-bands are next input to WSMO and evaluated using (5) and (6) to estimate $\{Z_1(\hat{\beta}_{\hat{k}}^*, f_{\hat{S}_{\hat{k}}}^*), Z_2(\hat{\beta}_{\hat{k}}^*)\}$. The bandwidth $\hat{\beta}_{\hat{k}}$ of fWSMO is variable and the computation of (5) requires additional summations and multiplications. The quantity $(1-\alpha)\, \dot{Z}_2(\hat{\beta}_{\hat{k}}, f_{\hat{S}_{\hat{k}}})$ therefore requires an additional $(\hat{K}^2 + \hat{K}) / 2$ multiplications (multiplication by 1-α), $(\hat{K}^2 + \hat{K}) / 2$ divisions (normalization of objective function), and $(\hat{K}^2 + \hat{K}) / 2$ summations (summation of the objective functions). The total number of multiplications and divisions of (5) now becomes $2(\hat{K}^2 + \hat{K})$. The number of summations needed for multi-objective optimization is $(3\hat{K}^2 + \hat{K}) / 2$ with $(5\hat{K}^2 + 7\hat{K}) / 2$ multiplications / divisions.

A. *Method to Identify Meso-Bands*

The method to identify meso-bands is illustrated by the state-space diagram in Fig. 6. The action assignments for each state transition are shown in Table I, where NA is the case when no transition occurs. Note that a minimal number of summations are needed for each state transition with no multiplications. The initialization state S_0 compares the first power sample θ_1 to T_f to determine if this power sample belongs to a low- or high-power meso-band. The binary variables $I_S \in \{0,1\}$ and $F_S \in \{0,1\}$ denote the initial and final transition states (0 for S_1, or 1 for S_2) and are used for the merging process. The state S_1 collects information on low-power meso-bands when $\theta_n < T_f$ and the state S_2 collects information on high-power meso-bands when $\theta_n \geq T_f$ (see Table I).

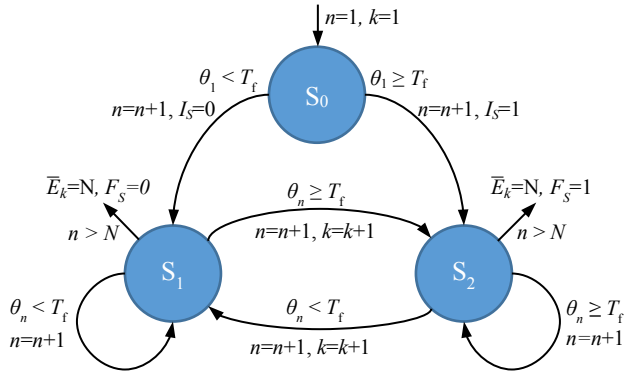

Fig. 6. State space model used to identify meso-bands in Θ.

Table I. Action table for the state space diagram of Fig. 6.

	n	k	$\bar{l}_k$	$\bar{T}_k$	$\bar{S}_k$	$\bar{E}_k$	Sum
IC	1	1	$\bar{l}_1=1$	$\bar{T}_1=\theta_1$	$\bar{S}_1=1$	NA	0
$S_0 \rightarrow S_1$ $S_0 \rightarrow S_2$	$n+1$	NA	NA	NA	NA	NA	1
$S_1 \rightarrow S_1$	$n+1$	NA	$\bar{l}_k=\bar{l}_k+1$	$\bar{T}_k=\bar{T}_k+\theta_n$	NA	NA	3
$S_1 \rightarrow S_2$	$n+1$	$k+1$	$\bar{l}_{k+1}=1$	$\bar{T}_{k+1}=\theta_n$	$\bar{S}_{k+1}=n$	$\bar{E}_k=n-1$	3
$S_2 \rightarrow S_1$	$n+1$	$k+1$	$\bar{l}_{k+1}=1$	$\bar{T}_{k+1}=\theta_n$	$\bar{S}_{k+1}=n$	$\bar{E}_k=n-1$	3
$S_2 \rightarrow S_2$	$n+1$	NA	$\bar{l}_k=\bar{l}_k+1$	$\bar{T}_k=\bar{T}_k+\theta_n$	NA	NA	3

B. *Method to Merge Meso-Bands*

The method to merge meso-bands is illustrated by the state-space diagram in Fig. 7, where the action assignments are shown in Table II. Once again, a minimal number of summations are needed for each state transition with no multiplications. Many of the summations needed for state transition are used for indexing purposes. The initialization state S_0 uses I_S to determine if the first meso-band is low- or high-power. If I_S equals 1, than the initial meso-band is high-power and the initial conditions are stored for a possible merge. If I_S equals 0, then state S_{01} is used to compare the low-power sub-band to the

threshold B_L. If $\bar{l}_k < B_L$, then the merging process begins in state S_2; otherwise, state S_1 cycles through the remaining low-power meso-bands until the condition $\bar{l}_k < B_L$ is achieved. For each state transition, the variable $k = k + 2$ is incremented and the condition $k > K$ checks if the bandwidths of all the meso-bands were examined. Once $k > K$ is true, the states S_3 through S_5 are used to finalize the merge process. States S_3 through S_5 are used to determine how the final meso-bands in Φ are to be added to $\hat{\Phi}$, where state S_3 adds both Φ_K and Φ_{K-1} to $\hat{\Phi}$ while states S_4 and S_5 add only Φ_K to $\hat{\Phi}$.

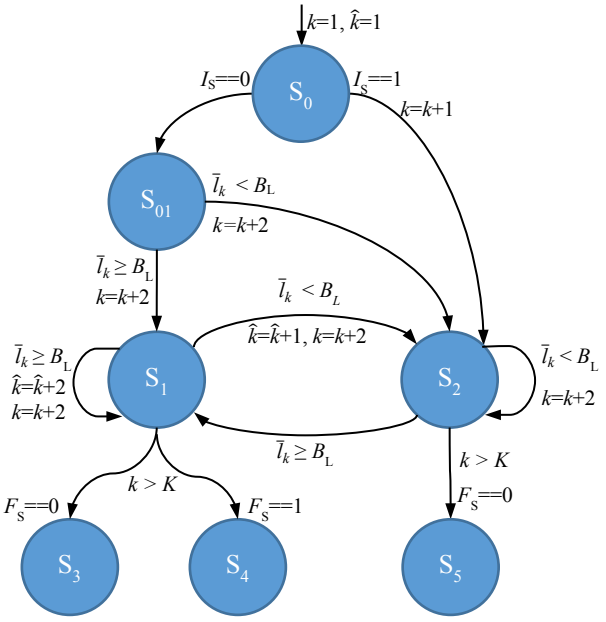

Fig. 7. State space model used to merge meso-bands in Φ.

Table II. Action table for the state space diagram in Fig. 7.

	k	$\hat{k}$	$\hat{\Gamma}_{\hat{k}}$	$\hat{S}_{\hat{k}}$	$\hat{E}_{\hat{k}}$	Sum
$S_0 \rightarrow S_2$	k+1	NA	$\hat{\Gamma}_{\hat{k}}=\bar{\Gamma}_k$	$\hat{S}_{\hat{k}}=\bar{S}_k$	$\hat{E}_{\hat{k}}=\bar{E}_k$	1
$S_{01} \rightarrow S_1$	k+2	NA	$\hat{\Gamma}_{\hat{k}}=\bar{\Gamma}_k$	$\hat{S}_{\hat{k}}=\bar{S}_k$	$\hat{E}_{\hat{k}}=\bar{E}_k$	1
$S_{01} \rightarrow S_2$	k+2	NA	$\hat{\Gamma}_{\hat{k}}=\bar{\Gamma}_k+\bar{\Gamma}_{k+1}$	$\hat{S}_{\hat{k}}=\bar{S}_k$	$\hat{E}_{\hat{k}}=\bar{E}_{k+1}$	2
$S_1 \rightarrow S_1$	k+2	$\hat{k}$+2	$\hat{\Gamma}_{\hat{k}+1}=\bar{\Gamma}_{k-1}$, $\hat{\Gamma}_{\hat{k}+2}=\bar{\Gamma}_k$	$\hat{S}_{\hat{k}+1}=\bar{S}_{k-1}$, $\hat{S}_{\hat{k}+2}=\bar{S}_k$	$\hat{E}_{\hat{k}+1}=\bar{E}_{k-1}$, $\hat{E}_{\hat{k}+2}=\bar{E}_k$	4
$S_1 \rightarrow S_2$	k+2	$\hat{k}$+1	$\hat{\Gamma}_{\hat{k}+1}=\bar{\Gamma}_{k-1}+\bar{\Gamma}_k+\bar{\Gamma}_{k+1}$	$\hat{S}_{\hat{k}+1}=\bar{S}_{k-1}$	$\hat{E}_{\hat{k}+1}=\bar{E}_{k+1}$	6
$S_2 \rightarrow S_1$	k+2	$\hat{k}$+1	$\hat{\Gamma}_{\hat{k}+1}=\bar{\Gamma}_k$	$\hat{S}_{\hat{k}+1}=\bar{S}_k$	$\hat{E}_{\hat{k}+1}=\bar{E}_k$	2
$S_2 \rightarrow S_2$	k+2	NA	$\hat{\Gamma}_{\hat{k}}=\hat{\Gamma}_{\hat{k}}+\bar{\Gamma}_k+\bar{\Gamma}_{k+1}$	NA	$\hat{E}_{\hat{k}}=\bar{E}_{k+1}$	4
$S_1 \rightarrow S_3$	NA	$\hat{k}$+2	$\hat{\Gamma}_{\hat{k}+1}=\bar{\Gamma}_{k-1}$, $\hat{\Gamma}_{\hat{k}+2}=\bar{\Gamma}_k$	$\hat{S}_{\hat{k}+1}=\bar{S}_{k-1}$, $\hat{S}_{\hat{k}+2}=\bar{S}_k$	$\hat{E}_{\hat{k}+1}=\bar{E}_{k-1}$, $\hat{E}_{\hat{k}+2}=\bar{E}_k$	3
$S_1 \rightarrow S_4$	k-1	$\hat{k}$+1	$\hat{\Gamma}_{\hat{k}+1}=\bar{\Gamma}_{k-1}$	$\hat{S}_{\hat{k}+1}=\bar{S}_{k-1}$	$\hat{E}_{\hat{k}+1}=\bar{E}_{k-1}$	2
$S_2 \rightarrow S_5$	NA	$\hat{k}$+1	$\hat{\Gamma}_{\hat{k}+1}=\bar{\Gamma}_k$	$\hat{S}_{\hat{k}+1}=\bar{S}_k$	$\hat{E}_{\hat{k}+1}=\bar{E}_k$	1

IV. Data Collection and Synthetic Spectra

Multiple RF spectra have been measured and used here for training and experimentation purposes. The spectra for training, i.e., the training set, are used to generate a set of synthetic spectra to train fWSMO in Section V. In this development, we assume generic knowledge of the expected EME and the synthetic data to be generated are comprehensive for training purposes. Extreme cases of RFI, not considered by the training set, would require a retraining of the algorithm. For all scenarios, training is performed offline and does not affect the computational complexity of SS-MO. The spectra for experimentation, i.e., the testing set, are used to compare WSMO and fWSMO in Section VI. A comprehensive set of measured data is needed to examine the capabilities of the proposed techniques. For example, such a comprehensive dataset should contain portions of spectra with 1) high-power narrowband interference, 2) wideband interference, 3) no interference (noise only), and 4) combinations of all types of interference. It is therefore necessary to collect spectral data with different power levels and spectral occupancy over a wide band of interest. The RF spectra considered in this analysis were collected between 100 MHz and 1 GHz, a band comprising various RF interference conditions.

The spectral data were collected with the measurement system in Fig. 8 using the Agilent Technologies N9342CN handheld spectrum analyzer [34] with an AOR DA3200 ultra-wideband discone antenna. The center frequency of the spectrum analyzer was swept from 100 to 900 MHz in 100 kHz increments (8000 sweeps total). For each sweep, a power spectrum was recorded with parameters: B = 100 MHz total bandwidth, Δ_r = 100 kHz, N = 1000 samples, a –30 dBm reference level, a 20 dB attenuation value, and no averaging. The average noise level, i.e. the noise floor, is specified in the data sheet as P_N = –92 dBm [34].

Fig. 8. Measurement system used to collect spectral data.

This sweep produces a set of 8000 recorded spectra. Each spectrum in the set is considered a separate trial to be processed by the optimization algorithms, where each trial contains a different measure of RFI and noise. The recorded spectra reflect a variety of spectral conditions used to examine the optimization algorithms. For example, consider one spectrum within the set with high-power narrowband interference, denoted Trial 1, and another with only noise (no RFI), denoted Trial 2. The optimization algorithms produce very different solutions for each trial. In Trial 1, the algorithms select a sub-band that avoids the narrowband RFI, while in Trial 2 they select the full bandwidth. The 8000 recorded spectra are defined as $\Psi = \{\Theta_1, \ldots, \Theta_{8000}\}$, where each $\Theta_\psi \in \Psi$ is a power spectrum that contains the power samples $\{\theta_{\psi,1}, \ldots, \theta_{\psi,1000}\}$ and $\psi \in \{1, \ldots, 8000\}$ is a variable denoting spectrum Θ_ψ.

Two sweeps (from 100 to 900 MHz) of the spectrum were conducted during experimentation, where each sweep produced 8000 spectra. The first sweep forms the training set and was conducted in the morning. The second sweep forms the experiment set and was conducted in the afternoon (same day). Using threshold $T_{\text{po}} = -89$ dBm, which is 3 dB above the –92 dBm noise floor, determines whether a given sub-band contains interference. The percent occupancy (PO) μ_ψ is computed as

$$\mu_\psi = \frac{1}{N}\sum_{n=1}^{N} y_{\psi,\,n} \times 100\%, \tag{11}$$

where

$$y_{\psi,\,n} = \begin{cases} 1, & \theta_{\psi,n} \geq T_{\text{po}} \\ 0, & \theta_{\psi,\,n} < T_{\text{po}} \end{cases}. \tag{12}$$

The percent occupancy for both the training and experiment sets is shown in Fig. 9, where it is observed that the training and experimental sets have similar occupancy. Also observe that the spectra have various RF interference conditions ranging from 2.5% to 55% POs.

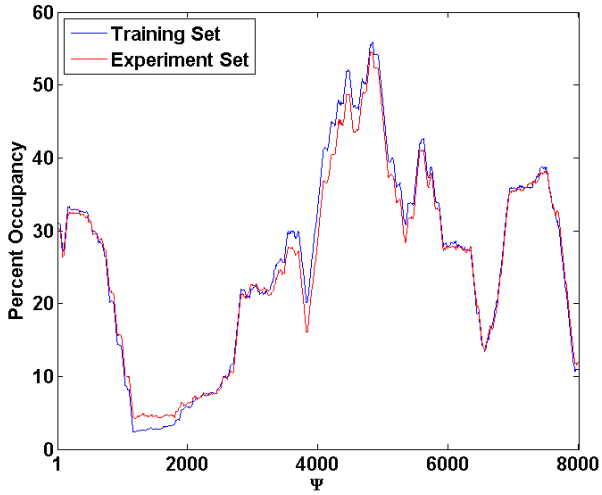

Fig. 9. Spectral occupancy of the measured data. The training and experiment sets were measured at different times.

The interference and noise power for both the training and experiment sets are shown in Fig. 10. The power for spectrum Θ_ψ is defined as

$$\bar{\theta}_\psi = \sum_{n=1}^{N} \theta_{\psi,\,n}. \tag{13}$$

Observe that the interference and noise power reflect multiple spectral categories including the noise floor, high-power narrowband interference, wideband interference, and combinations thereof. The power of the narrowband interference in Θ_{2900} is 27 dB greater than the noise floor measured in Θ_{1900}. The bandwidth of the wideband interference for the spectra between Θ_{4000} and Θ_{5000} is 23.6 MHz.

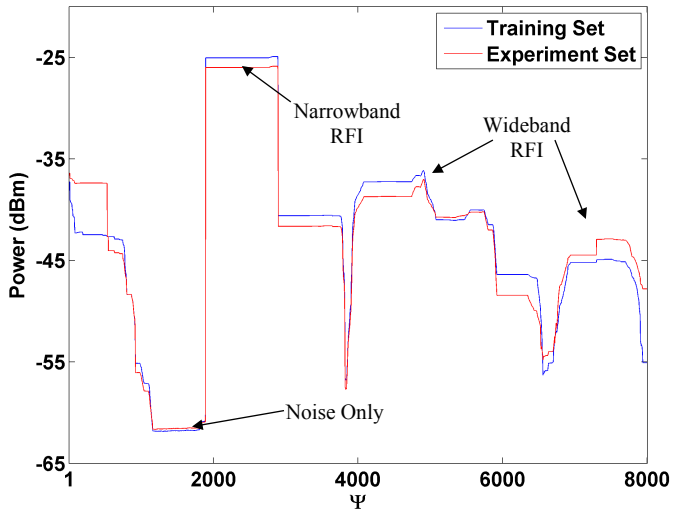

Fig. 10. Interference and noise power of the measured data that reflects a variety of spectral categories.

The training data are used to train the parameters of fWSMO and are further examined using the histogram shown in Fig. 11. Although the training data represent a variety of spectral categories (as discussed previously), spectra are very similar for particular categories. For example, 631 spectra represent the noise only case while 246 spectra represent narrowband RFI. The histogram further illustrates gaps between categories of spectra. To analyze the best- and worst-case performance of fWSMO, a more comprehensive synthetic training set is required that fills the gaps between the categories.

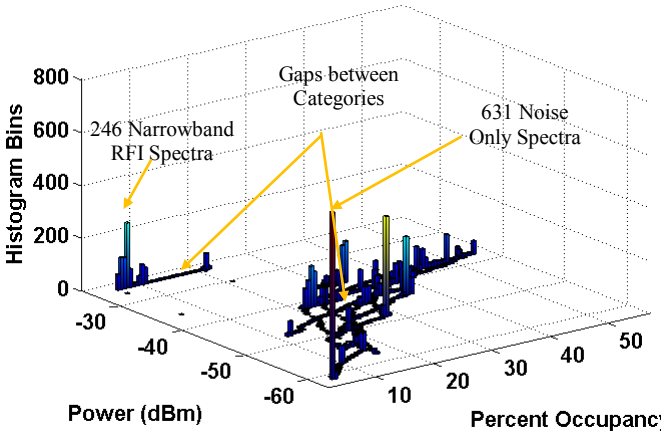

Fig. 11. Histogram of training set. Observe that several spectra are very similar for particular categories.

The synthetic data are created based on the observations of the measured data; otherwise, the synthetic data would be overwhelmingly large and not represent real-world scenarios. The observations are based on the following five PO levels: 0 to 10%, 10 to 20%, 20 to 30%, 30 to 40%, and 40 to 50%. Note that the PO above 50% is not considered since only a small number of spectra fit into this category. For each PO level, fundamental spectrum templates (FSTs) are used to randomly replicate the RFI at different frequency and power levels. Three FSTs are designed to represent narrowband interference, wideband interference, or the noise floor. The narrowband FST is defined using a simple sinusoid:

$$X_s(t) = A_s \cos(2\pi f_s t), \quad (14)$$

where $A_s = \sqrt{P_s}$ and f_s are uniform random variables of the amplitude and frequency, respectively; $0 \le t \le T$, $T = 1 / \Delta_r$; and $0 \le f_s \le B$. P_s is the power of the signal amplitude with $P_{s,l} \le P_s \le P_{s,u}$. The wideband FST is defined by a linear frequency modulated chirp waveform:

$$X_c(t) = A_c \cos(2\pi f_c t + \pi[B_c / \tau]\, t^2), \quad (15)$$

where $A_c = \sqrt{P_c}$, f_c, and B_c are uniform random variables of the amplitude, frequency, and bandwidth respectively. The lower and upper limits of the random variables are $B_c / 2 \le f_c \le B - B_c / 2$, and $B_{c,l} \le B_c \le B_{c,u}$. P_c is the power of the signal amplitude with $P_{c,l} \le P_c \le P_{c,u}$. The signal used to estimate the synthetic spectrum is

$$X(t) = X_s(t) + X_c(t) + X_n(t), \quad (16)$$

where $X_n(t)$ is additive white Gaussian noise designed to produce a noise floor similar to the measured data. The power spectrum of (16) is then estimated using $\Phi(\bullet)$ (Fourier transform) with the same parameters defined for the measured data, e.g., Δ_r = 100 kHz, N = 1000 samples, and B = 100 MHz.

Tables III–V summarize the design criteria used to generate the synthetic spectra. The design criteria are chosen based on the observations of the power spectra in the training set. No attempt was made to identify the RF system type since only the power spectrum is available for observation. The top row in each table indicates the number of spectra generated, number of wideband (WB) signals per spectrum, number of narrowband (NB) signals per spectrum, the signal power used in (14) and (15), and the bandwidth used in (15). A total of 5000 spectra are generated, 1000 spectra for each PO level. A row split indicates two or more FSTs of the same type with different parameters. For example the row split in row 5, column 3 of Table III indicates 1 to 9 randomly generated sinusoids with $-85 \le P_s \le -75$ dBm using (14), and 1 sinusoid with $P_s \approx -27$ dBm using (14) (Fig. 12).

Table III summarizes the design criteria for spectra with a PO level between 0 – 10%. these design criteria are based on the following observations: 1) noise only (row 2), 2) 1 wideband signal with $5 \le B_c \le 6$ MHz and $-78 \le P_c \le -72$ dBm (row 3), 3) 1 to 9 narrowband signals with $-85 \le P_s \le -75$ dBm and 1 wideband signal with $0.5 \le B_c \le 1$ MHz and $-78 \le P_c \le -72$ dBm (row 4), and 4) identical to observation 3 plus high-power narrowband interference with $P_s \approx -27$ dBm. An example of the RFI observed for case 4 is illustrated in Fig. 12. Table IV summarizes the design criteria for spectra with a PO level between 10 – 20%. Row 2 reflects observations of 2 wideband signals per spectrum. Rows 3 and 5 reflect observations of random sinusoids in the presence of 1 wideband signal. Row 4 reflects observations of 3 wideband signals per spectra in the presence of multiple sinusoids.

Table III. Spectral design criteria for PO levels between 0 – 10%.

Total Spectra	NB	P_s (dBm)	WB	P_c (dBm)	B_c (MHz)
100	0	0	0	0	0
300	0	0	1	-78 to -72	5 to 6
300	1:9	-85:-75	1	-78:-72	0.5:1
300	1:9	-85:-75	1	-78:-72	0.5:1
	1	-27			

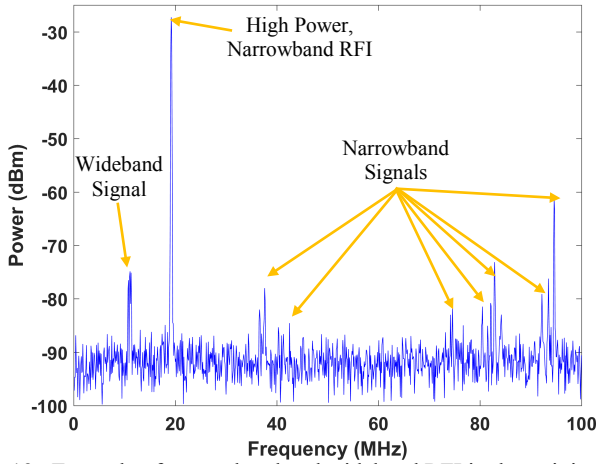

Fig. 12. Example of narrowband and wideband RFI in the training set.

Table IV. Spectral design criteria for PO levels between 10 – 20%.

Total Spectra	NB	P_s (dBm)	WB	P_c (dBm)	B_c (MHz)
250	0	0	2	-78:-72	5:6
250	8:12	-85:-60	1	-78:-72	0.5:1
	1	-27			
250	7:8	-88:-77	1	-86:-82	11:12
			1	-78:-72	5:6
			1	-88:-84	2:3
250	6:10	-88:-61	1	-78:-72	8:9

Table V summarizes the design criteria for spectra with a PO level between 20–50%. A PO level between 20–30% reflects observations of 3 to 4 wideband signals present in the spectrum (Row 2), and multiple random sinusoids in the presence of 1 wideband signal (Row 3). A PO level between 30–40% reflects observations of 4 to 6 wideband signals (Row 4); or 2 wideband signals per spectrum (Row 5). A PO level between 40–50% reflects observations of multiple wideband signals in the presence of a 24 MHz wideband signal. The histogram of the synthetic data is shown in Fig. 13. The histogram illustrates a comprehensive training set that fills the gaps between the categories in Fig. 11. The 5000 synthetic spectra are defined as $\Psi_S = \{\Omega_1, \ldots, \Omega_{5000}\}$, where each $\Omega_\psi \in \Psi_S$ is a power spectrum that contains the power samples $\{\omega_{\psi,1}, \ldots, \omega_{\psi,1000}\}$ and $\psi \in \{1, \ldots, 5000\}$ is a variable denoting the spectrum Ω_ψ.

Table V. Spectral design criteria for PO levels between 20 – 50%.

PO	Total Spectra	NB	P_s (dBm)	WB	P_c (dBm)	B_c (MHz)
20-30	750	0:11	-80:-40	3:4	-85:-60	5:6
20-30	250	10:15	-85:-60	1	-63:-58	11:12
30-40	750	0:10	-80:-40	4:6	-80:-65	6:7

30-40	250	0	0	1	-70:-55	24:25
				1	-85:-75	6:7
40-50	1000	0	0	4:5	-80:-65	5:6
				1	-80:-65	24

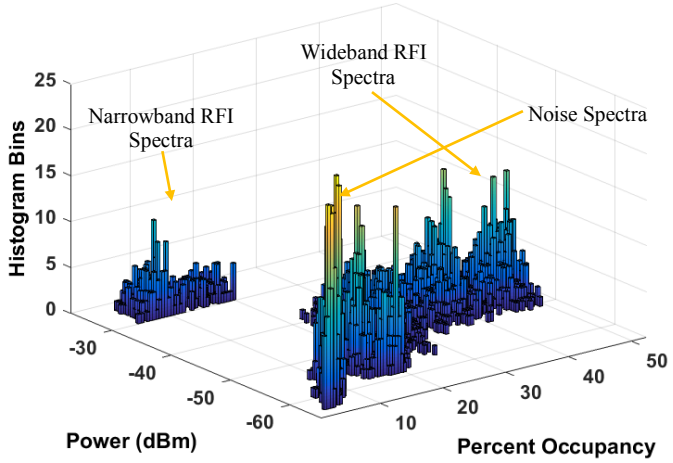

Fig. 13. Histogram of synthetic data.

V. Parameter Selection for Fast WSMO

The training set is used to examine the performance of fWSMO for different values of T_f and B_f. To examine the trade-off between SINR and bandwidth, the performance is measured using a distance metric that quantifies the error between $\{Z_1(\hat{\beta}_k^*, \hat{f}_k^*),\ Z_2(\hat{\beta}_k^*)\}$ and $\{Z_{1,\max}, Z_{2,\max}=B\}$. $Z_{1,\max}$ is found exhaustively (without meso-bands) using (5) since training is performed offline. Therefore, the best available SINR is used in the evaluation of the parameter selection. The distance metric for the spectrum Ω_ψ is defined as

$$D_\psi = \frac{Z_{1,\max} - Z_1(\hat{\beta}_k^*, \hat{f}_k^*)}{Z_{1,\max}} + \frac{B - Z_2(\hat{\beta}_k^*)}{B}, \qquad (17)$$

which is used as the primary evaluation criterion for the parameters of fWSMO. Note that (17) follows the L_p distance where $p = 1$, a metric commonly referred to as the Manhattan distance [35]. This metric is considered since it measures linear distance, which is needed to properly examine the results of linearly combining the objective functions.

The fWSMO approach is used to process each spectrum in Ψ_S to generate the set of distances, $\{D_1, \ldots, D_{5000}\}$ and is evaluated using each of the input parameters $T_f \in \{-90, -89, \ldots, -70\}$ dBm and $B_f \in \{0.1, 0.2, \ldots, 4.0\}$ MHz. The goal of this examination is to find T_f^* and B_f^* that result in a high performance, low complexity implementation of fWSMO.

fWSMO uses the following parameters for training: $Z_{1,\min} = -10$ dB for SINR, $Z_{2,\min} = 5$ MHz for bandwidth, and $C = 2\times10^{-19}$ as the radar range equation constant. It should be noted that these parameters are selected to test the capabilities of fWSMO for an arbitrary radar type and application. The boundary conditions are set low so that multiple sub-band choices are available to fWSMO. The weighting parameter for WSMO is selected as $\alpha = 0.5$ so that each objective function is given equal priority. The radar range equation constant is selected arbitrarily so that the maximum SINR is 15 dB.

The fWSMO approach is used to process spectrum Ω_d for each combination of T_f and B_f, resulting in $G = 840$ different evaluations of fWSMO for spectrum ψ: $\{D_{\psi,1}, \ldots, D_{\psi,840}\}$. The average distance is then found each parameter combination g, $\sum_{\psi=1}^{5000} D_{\psi,g}/5000$, with the results shown in Fig. 14. Note that a high T_f results in a small number meso-bands, $K << N$, since the majority of the RFI is below the threshold. The number of decision variables needed to form the solution space are therefore inadequate and the optimal solution is not reached. A high B_f bandwidth increases the number of merged meso-bands, again resulting in a limited number of decision variables. The parameter combination that produces the smallest error is $T_f = -88$ and $B_f = 0.1$, which is expected since a large number of meso-bands exist and $K \approx N$.

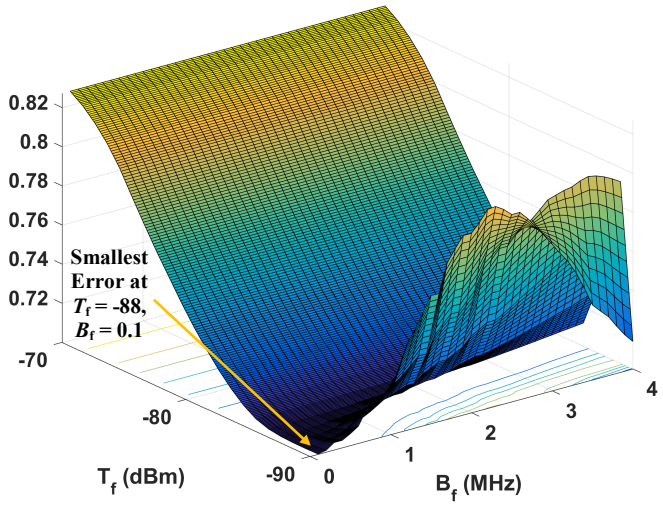

Fig. 14. Average L_1 distance measure of synthetic data.

The secondary criterion used to evaluate the parameters of fWSMO is computational complexity, for which the number of summations and multiplications are examined. The evaluation that follows only considers the number of summations since the results for the number of multiplications are similar. Similar to the average distance, the number of summations are measured for each combination of T_f and B_f whose results are shown in Fig. 15. Clearly a low threshold and bandwidth result in a high computational complexity since a large number of meso-bands exists and $K \approx N$; however, as discussed, a low threshold and bandwidth also result in high performance. The compromise is to combine, and jointly evaluate, the information in Figs. 13 and 14. The information is combined by normalizing and then summing the results shown in each plot. The combined information is shown in Fig. 16 where the parameters of the minimum value are $T_f^* = -86$ dBm and $B_f^* = 0.7$ MHz.

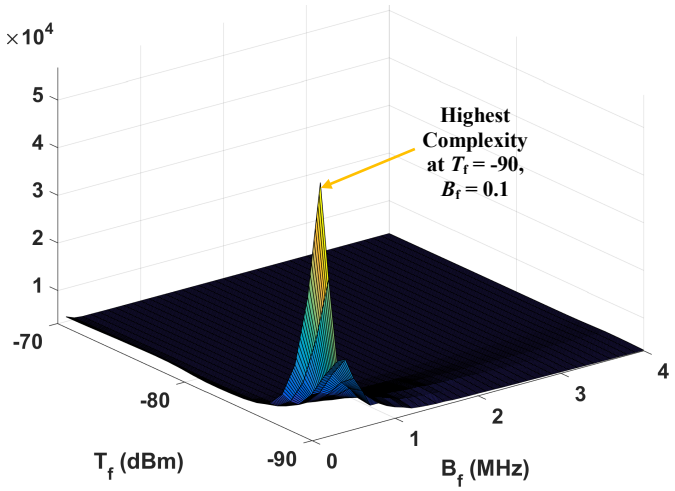

Fig. 15. Number of summations generated by fWSMO.

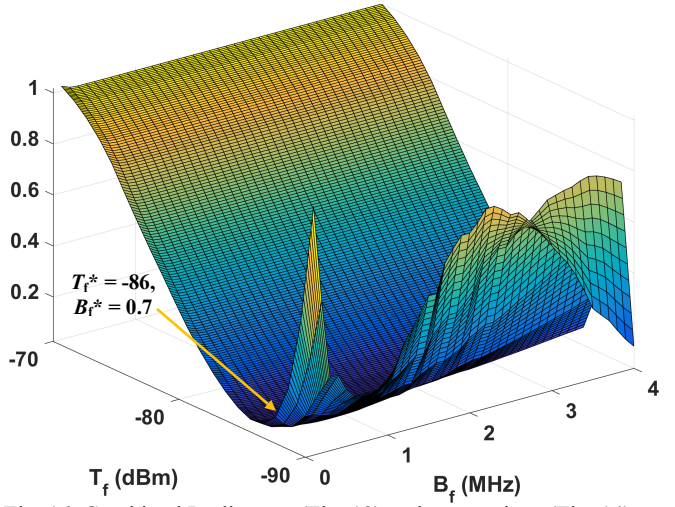

Fig. 16. Combined L_1 distance (Fig. 13) and summations (Fig. 14).

VI. Experiment and Algorithm Comparison

Here we consider the application of WSMO and fWSMO to the experimental data. Recall that the algorithm parameters are defined as $Z_{1,\min} = -10$ dB, $Z_{2,\min} = 5$ MHz, $C = 2\times10^{-19}$, $\alpha = 0.5$, $T_f = -86$ dBm, and $B_f = 0.7$ MHz. Performance is measured and compared for 1) full bandwidth (FB) B, representing standard radar operation with no spectrum sensing; 2) WSMO; and 3) fWSMO. The SINR of the processed spectra is shown in Fig. 17. Three traces are illustrated: 1) FB – dash-dot red, 2) WSMO – solid blue, 3) fWSMO – dashed green. The average SINR is also estimated for each technique, where the FB average SINR is 5.29 dB, the WSMO average SINR is 13.41 dB, and the fWSMO average SINR is 13.4 dB. The FB method produces some results below $Z_{1,\min}$ indicating non-feasible solutions. In contrast, WSMO and fWSMO meet the SINR boundary limit requirements for all processed spectra and indicate a significant increase in SINR. Also observe that the SINRs between fWSMO and WSMO are very similar, a result validated by the average SINR where the difference between WSMO and fWSMO is only 0.01 dB. There exist only three exceptions to this observation; they are discussed in detail next.

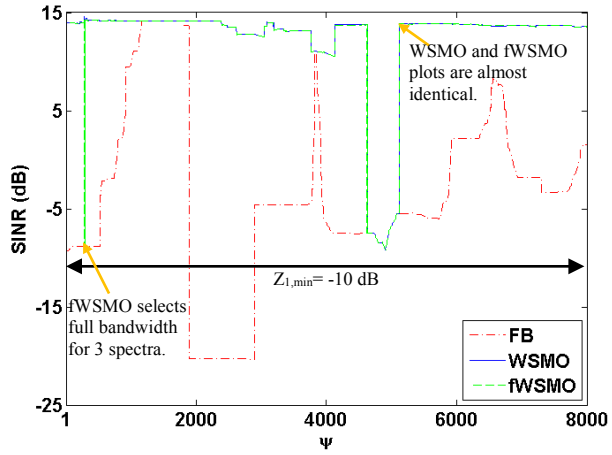

Fig. 17. SINR results for FB, WSMO, and fWSMO. The FB average SINR is 5.29 dB, the WSMO average SINR is 13.41 dB, and the fWSMO average SINR is 13.4 dB.

The L_1 distance measure is shown in Fig. 18 where WSMO and fWSMO outperform FB, a result further justifying the SS-MO technique. Three traces are illustrated: 1) FB – dash-dot red, 2) WSMO – solid blue, 3) fWSMO – dashed green. The average L_1 distance is also estimated for each technique, where the FB average is 0.8874, the WSMO average is 0.6750, and the fWSMO average is 0.6757. WSMO serves as the L_1 distance measure lower bound. The results for fWSMO are very similar to WSMO, where the difference between the average L_1 distance measures (blue and green dashed) is only 0.0007.

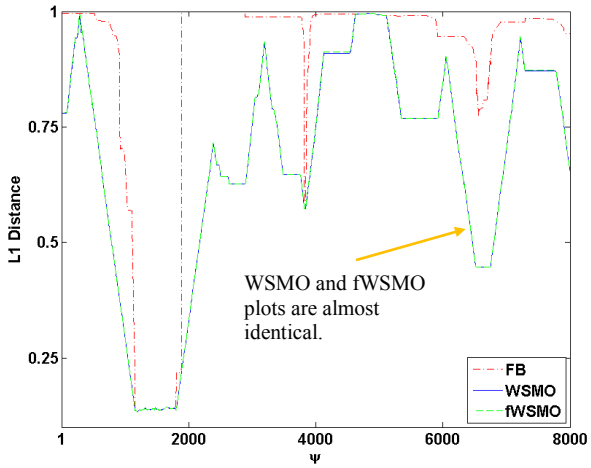

Fig. 18. Distance measure results for FB, WSMO, and fWSMO. The average L1 distance for FB is 0.8874, WSMO is 0.6750, and fWSMO is 0.6757. The difference between WSMO and fWSMO is 0.0007.

As depicted in Fig. 17, SINR for fWSMO is degraded for 3 spectra at Θ_{283}, Θ_{284}, and Θ_{287}. Closer examination of Θ_{283} in Fig. 19 shows that fWSMO selects the full-bandwidth solution whereas WSMO selects a smaller band. This difference is caused by the fWSMO bandwidth merge process (Section III-B). The merge process combines the meso-bands, resulting in a limited number of decision variables and a smaller solution

space. For example, the sub-band selected by WSMO (blue) in Fig. 19 is in a valley between two RFI peaks. Since the peaks are above the threshold T_f = -86 dBm, the merge process combines all frequency bins between the peaks. This merged sub-band has added RFI power that results in lower SINR (as compared with WSMO), which causes fWSMO to select the full-bandwidth solution. This result is analogous to processing with a coarse frequency resolution (fWSMO) compared to a fine frequency resolution (WSMO).

It should also be noted that the WSMO sub-band in Fig. 19 is 5 MHz, which equals the boundary condition for a feasible solution. The L_1 distance in Fig. 18 illustrates very similar error between fWSMO and WSMO (a difference of only 0.0007), meaning that both techniques have very similar performance trade-off characteristics. So the question remains as to which choice is better, enhanced range resolution or high SINR? The answer to this question is application / scenario dependent and is beyond the scope of this analysis.

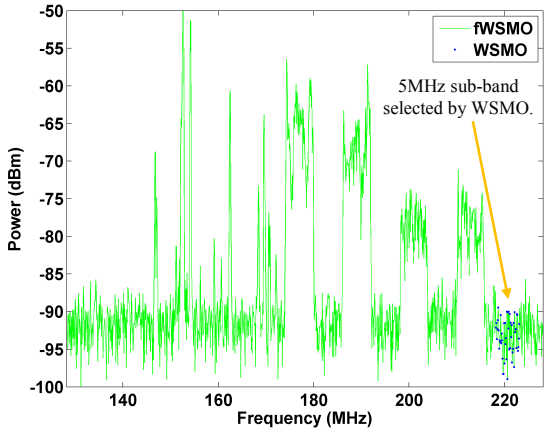

Fig. 19. Spectrum Θ_{283} shows that fWSMO selects the full bandwidth to enhance range resolution while WSMO selects a 5 MHz sub-band to enhance SINR.

The computational complexity of WSMO and fWSMO are compared in Fig. 20. The results indicate that the computational complexity of fWSMO is $O(N)$ for both summations and multiplications; a result significantly less than that of WSMO. The average number of summations used by fWSMO is 4070 and is consistent for each spectrum in Ψ. The number of multiplications fluctuate between 85 and 3397, with an average of 1644. The multiplications drop significantly for spectra between Θ_{1152} and Θ_{1821} (noise only), which is due to the small number of merged meso-bands, i.e., only 1 sub-band exists (the full bandwidth) resulting in a minimum number of multiplications. The number of summations and multiplications needed for WSMO are 1×10^6 and 1.5×10^6 respectively. In comparison, fWSMO reduces the number of summations by a factor of approximately 245 and the number of multiplications by a factor of 912. These results demonstrate that fWSMO significant reduces the computational complexity, resulting in faster analysis of the data by multi-objection optimization. fWSMO, in essence, serves as a "filter" that removes redundant information in the spectrum. As discussed in the introduction, this process is analogous to the information reduction process that occurs in the thalamus, which likewise serves as a "filter" that reduces external stimuli before it is processed by other areas in the human brain [30].

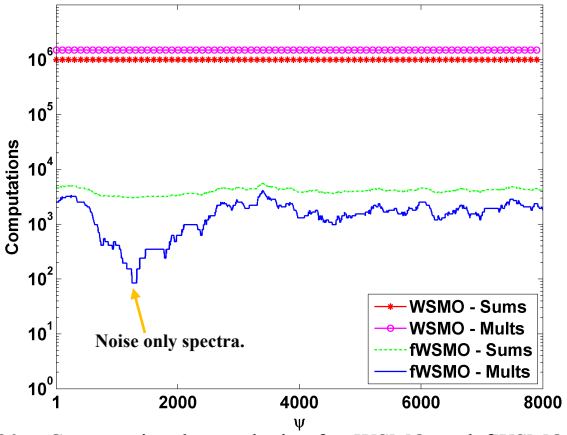

Fig. 20. Computational complexity for WSMO and fWSMO. The number of summations and multiplications needed for fWSMO is significantly less than that needed for WSMO.

VII. Conclusions

Two multi-objective optimization approaches have been investigated for the SS-MO technique. The results indicate that using the full bandwidth (without SS-MO) in the presence of RFI results in reduced SINR. In contrast, WSMO and fWSMO both meet the SINR boundary limit requirements for various measured spectra and produce significantly lower distances. These results justify the utility of the SS-MO technique for radar in a spectrally congested environment.

The SINR and distance performance measures of fWSMO were very similar to WSMO. Empirical analysis indicated that the solution space for fWSMO is slightly smaller than that for WSMO due to the sub-band merging process. The computational complexity of fWSMO was found to be $O(N)$ for both summations and multiplications. A comparison between WSMO and fWSMO shows that the latter realizes orders of magnitude reduction in computational cost. Both performance and complexity results suggest that fWSMO is the best trade-off between the evaluated techniques. Future work will consider investigation of fWSMO to particular radar scenarios of interest for different RFI conditions. The goal of this investigation is to study how the parameter selections of fWSMO change between the different RFI conditions. This investigation may also lead to the development of a more general framework for the selection of fWSMO parameters for different radar scenarios of interest. Once the radar scenario is defined and the hardware architecture is known, a detailed examination of the time parameters (T_C, T_S, T_{MO}, and T_R) can also be investigated and a direct comparison of CPI time and radar performance can be evaluated. Other future investigations will examine SS-MO for notched waveform applications, such as those discussed in [12, 13, 19-23]. The notched waveform applications require an extension for SS-MO to identify multiple disjoint sub-bands. These investigations will examine techniques to identify the local maxima of the SS-MO solutions and the associated computational complexity required to implement the approach.

REFERENCES

[1] H. Griffiths, L. Cohen, S. Watts, E. Mokole, C. Baker, M. Wicks, and S. Blunt, "Radar spectrum engineering and management: technical and regulatory issues," *Proc. IEEE*, vol. 103, no. 1, pp. 85-102, Jan. 2015.

[2] A.F. Martone, "Cognitive radar demystified," *URSI Bulletin,* no. 350, pp. 10-22, Sept. 2014.

[3] Z. Geng, H. Deng, and B. Himed, "Adaptive radar beamforming for interference mitigation in radar-wireless spectrum sharing," *IEEE Signal Processing Letters*, vol. 22, no. 4, pp. 484-488, Apr. 2015.

[4] Federal Communication Commission, "Auction of advanced wireless services (AWS-3) licenses closes," Wash. D.C., DA 15-131, 2015.

[5] T. Higgins, T. Webster, and A.K. Shackelford, "Mitigating interference via spatial and spectral nulling," *IET Radar, Sonar & Navigation*, vol. 8, no. 2, pp. 84–93, 2014.

[6] K. Gerlach, "Thinned spectrum ultrawideband waveforms using stepped-frequency polyphase codes," *IEEE Transactions on Aerospace and Electronic Systems*, vol. 34, no. 4, pp. 1356–1361, Oct. 1998.

[7] M. Labib, J.H. Reed, A.F. Martone, A.I. Zaghloul, "Coexistence between radar and LTE-U systems: survey on the 5 GHz band," in *USNC-URSI Radio Science Meeting*, Boulder, CO, Jan. 2016.

[8] J.M. Peha, "Sharing spectrum through spectrum policy reform and cognitive radio," *Proc. IEEE*, vol. 97, no. 4, pp. 708-719, Apr. 2009.

[9] H. Wang, J. Johnson, C. Baker, L. Ye, and C. Zhang, "On spectrum sharing between communications and air traffic control radar systems," *IEEE Intl. Radar Conf.*, Arlington, VA, pp. 1545-1550, May 2015.

[10] R. Saruthirathanaworakun, J.M. Peha, and L.M. Correia, "Opportunistic primary-secondary spectrum sharing with a rotating radar," *Intl. Conf. Computing, Networking and Communications,* Maui, HI, pp. 1025-1030, Jan./Feb. 2012.

[11] S.S. Bhat, R.M. Narayanan, and M. Rangaswamy, "Bandwidth sharing and scan scheduling in multimodal radar with communications and tracking," *IETE Journal of Research*, vol. 59, no. 5, pp. 551–562, Sept. 2013.

[12] J. Jakabosky, S.D. Blunt, and A.F. Martone, "Incorporating hopped spectral gaps into nonrecurrent nonlinear FMCW radar emission," *IEEE Intl. Workshop Computational Advances in Multi-Sensor Adaptive Processing*, Cancun, Mexico, pp. 281-284, Dec. 2015.

[13] J. Jakabosky, B. Ravenscroft, S.D. Blunt, and A.F. Martone, "Gapped spectrum shaping for tandem-hopped radar/communications & cognitive sensing," *IEEE Radar Conf.*, Philadelphia, PA, May 2016.

[14] A. Khawar, A. Abdel-Hadi, and T.C. Clancy, "Spectrum sharing between S-band radar and LTE cellular system: A spatial approach," *IEEE Intl. Symp. Dynamic Spectrum Access Networks,* Mclean, VA, pp. 1-4, Apr. 2014.

[15] M.A. Govoni, H. Li, and J.A. Kosinski, "Low Probability of Interception of an advanced noise radar waveform with linear-FM," *IEEE Transactions on Aerospace and Electronic Systems*, vol. 49, no. 2, pp. 1351-1356, Apr. 2013.

[16] J.G. Metcalf, C. Sahin, S.D. Blunt, and M. Rangaswamy, "Analysis of symbol design strategies for intrapulse radar-embedded communications," *IEEE Trans. Aerospace & Electronic Systems*, vol. 51, no. 4, pp. 2914-2931, Oct. 2015.

[17] P. Stinco, M.S. Greco and F. Gini, "Spectrum sensing and sharing for cognitive radars," *IET Radar, Sonar & Navigation*, vol. 10, no. 3, pp. 595-602, Feb. 2016.

[18] E. Axell, G. Leus, E. Larsson, and V. Poor, "Spectrum sensing for cognitive radio: state-of-the-art and recent advances," *IEEE Signal Processing Magazine*, vol. 29, no. 3, pp. 101-116, May 2012.

[19] M.J. Lindenfeld, "Sparse frequency transmit-and-receive waveform design," *IEEE Trans. Aerospace & Electronic Systems,* vol. 40, no. 3, pp. 851-861, July 2004.

[20] M.R. Cook, T. Higgins, A.K. Shackelford, "Thinned spectrum radar waveforms," *Intl. Waveform Diversity & Design Conf.*, Niagara Falls, ON, Canada, Aug. 2010.

[21] K. Gerlach, M.R. Frey, M.J. Steiner, A. Shackelford, "Spectral nulling on transmit via nonlinear FM radar waveforms," *IEEE Trans. Aerospace & Electronic Systems*, vol. 47, no. 2, pp. 1507-1515, Apr. 2011.

[22] C. Nunn, L.R. Moyer, "Spectrally-compliant waveforms for wideband radar," *Aerospace & Electronic Systems Mag.,* vol. 27, no. 8, pp. 11-15, August 2012.

[23] A. Aubry, A. De Maio, Y. Huang, M. Piezzo, A. Farina, "A new radar waveform design algorithm with improved feasibility for spectral coexistence," *IEEE Trans. Aerospace & Electronic Systems*, vol. 51, no. 2, pp. 1029-1038, Apr. 2015.

[24] A.F. Martone, K.A. Gallagher, K.D. Sherbondy, A. Hedden, and C. Dietlein, "Adaptable waveform design for enhanced detection of moving targets," *IET Radar, Sonar, & Navigation, In Press.*.

[25] A.F. Martone, K.D. Sherbondy, K.I. Ranney, and T.V. Dogaru, "Passive sensing for adaptable radar bandwidth," *IEEE Intl. Radar Conf.*, Arlington,Va, May 2015.

[26] A.F. Martone, K.A. Gallagher, K.D. Sherbondy, K.I. Ranney, T.V. Dogaru, G.J. Mazzaro, and R.M. Narayanan, "Adaptable bandwidth for harmonic step-frequency radar," *International Journal of Antennas and Propagation*, Article ID 808093, July 2015.

[27] R.K. Pooler, "An analysis of spectrum sharing for radar applications," M.S. thesis, Department of Electrical Engineering, The Pennsylvania State University, State College, PA, December 2016.

[28] A.F. Martone, K.D. Sherbondy, and K.I. Ranney, "Genetic algorithm for adaptable radar bandwidth," *IEEE Radar Conf.*, Philadelphia, PA, May 2016.

[29] A.F. Martone, and K. Ranney, "Fast technique for wideband spectrum sensing," in *IEEE Intl. Symp. on Antennas and Propagation*, Memphis, Tennessee, July 2014.

[30] W.M. Connelly, M. Laing, A.C. Errington, and V. Crunelli, "The thalamus as a low pass filter: filtering at the cellular level does not equate with filtering at the network level," *Frontiers in Neural Circuits*, vol. 9, no. 89, pp. 1–10, Jan. 2016.

[31] N.C. Andreasen, S. Arndt, V. Swayze, T. Cizadlo, M. Flaum, D. O'Leary, W.T. Yuh, "Thalamic abnormalities in schizophrenia visualized through magnetic resonance image averaging," *Science*, vol. 266, no. 5183, pp. 294-298, Oct. 1994.

[32] A.R. Gilbert, D.R. Rosenberg, K. Harenski, S. Spencer, J.A. Sweeney, M.S. Keshavan, "Thalamic volumes in patients with first-episode schizophrenia," *American Journal of Psychiatry*, vol. 158, no. 4, pp. 618-624, April 2001.

[33] A. Konaka, D. Coitb, and A. Smith, "Multi-objective optimization using genetic algorithms: a tutorial," *Reliability, Engineering, and System Safety*, vol. 91, no. 9, pp. 992-1007, September 2006.

[34] *Agilent N9342C handheld spectrum analyzer (HAS) 7 GHz data sheet*, www.agilent.com/find/N9342C, Agilent Technologies, May 2014.

[35] R. Duda, P. Hart, and D. Stork, "Metrics and nearest neighbor classification," in *Pattern classification*. New York, NY: John Wiley & Sons, 2001, ch. 4, sec. 4.6, pp. 187 – 188.

Anthony F. Martone received the B.S. degree in electrical engineering from Rensselaer Polytechnic Institute (*Summa Cum Laude*), Troy, New York in 2001 and the Ph.D. degree in electrical engineering from Purdue University, West Lafayette, Indiana in 2007. Dr. Martone joined the U.S. Army Research Laboratory (ARL) in Adelphi, Maryland in 2007 as a researcher in the RF Signal Processing and Modeling branch where his research interests include sensing through the wall technology, spectrum sharing, and radar signal processing. He is currently the Sensors and Electron Devices Directorate lead for Cognitive Radar research where he is overseeing, directing, and collaborating with multiple universities to address spectrum sharing for radar and communication systems, software defined transceiver control, and adaptive processing techniques.

Since joining ARL Dr. Martone has authored over 70 journal and conference publications, 2 book chapters, and 6 patents. He received the Commanders Award for Civilian Service in December 2011 for his research and development of sensing through the wall signal processing techniques and has served as a committee member for graduate students at The Pennsylvania State University and the Virginia Polytechnic Institute and State University. Dr. Martone was elected to Senior Member of the IEEE in July 2013 and is an Associate Editor for the IEEE Transactions on Aerospace and Electronic Systems.

Kenneth I. Ranney (M'04–SM'09) received the B.S. degree in electrical engineering and computer science from The Johns Hopkins University, Baltimore, MD, USA, and the M.S. degree in electrical engineering from the University of Maryland at College Park, College Park, MD, USA. He is currently a Senior Research Engineer with the Army Research Laboratory, Adelphi, MD, USA, focusing on problems related primarily to radar signal processing and automatic target detection. He has authored or co-authored several journal articles and holds multiple patents. Mr. Ranney serves as the Co-Chair of the Radar Sensor Technology Conference within the SPIE Defense + Commercial Sensing Symposium.

Kelly D. Sherbondy is the System Design and Experimentation Team Leader, RF Signal Processing & Modeling Branch, Electronics and RF Division, Sensor & Electron Devices Directorate (SEDD), Army Research Laboratory (ARL), Research Development & Engineering Command (RDECOM). His interests are in basic, applied & systems research in Improvised Explosive Device (IED), Landmine and Unexploded Ordnance (UXO) detection. Within SEDD, Kelly is the Counter -IED (CIED) Subject Matter Expert (SME) lead. He is also a core member of the Office of Secretary of Defense (OSD)/Joint IED Defeat Organization (JIEDDO) CIED Science & Technology (S&T) Community of Interest (COI). Prior to ARL, he worked four years as the RDECOM CIED Task Force Chair and one year as the RDECOM CIED liaison to JIEDDO. Before becoming the RDECOM CIED TF Chair, he was a Deputy Countermine Division Chief and prior to that an S&T Countermine Branch Chief for the Night Vision and Electronic Sensors Directorate (NVESD) within the Communications & Electronic Research Development and Engineering Center (CERDEC). He holds three patents and has authored over 50 technical papers in CM & CIED technologies. Kelly has received the CERDEC Award for Employee of the Year (mid-level management) 2005, Award for Excellence (Management) 2005, Commander's Award for Civilian Service – CERDEC 2008, Commendation of Achievement – NVESD (2009) & ARL (2012), ARL-SEDD Recognition for Excellence 2010, 2011 and 2012. kelly.d.sherbondy.civ@mail.mil

Kyle A. Gallagher received the B.S., M.S., and Ph.D. degrees in electrical engineering from The Pennsylvania State University, in 2011, 2013, and 2015, respectively. He is currently an Electronic Engineer with the U.S. Army Research Laboratory, Adelphi, MD, USA. His research interests are ultra-wideband radar, nonlinear radar, and cognitive radar.

Shannon D. Blunt (S'96—M'02—SM'07—F'16) received the Ph.D. degree in electrical engineering from the University of Missouri in 2002. From 2002 to 2005 he was with the Radar Division of the Naval Research Laboratory in Washington, D.C. Since 2005 he has been with the Department of Electrical Engineering and Computer Science at the University of Kansas where he is currently a Professor and Director of the Radar Systems & Remote Sensing Lab (RSL).

In 2012 Prof. Blunt received the IEEE/AESS Nathanson Memorial Radar Award and in 2008 received the AFOSR Young Investigator Award. He has over 120 refereed journal and conference publications, 11 patents, and 7 book chapters. He co-edited the book *Principles of Waveform Diversity & Design* and is co-editing the upcoming book *Radar & Communication Spectrum Sharing*.

He is a member of the IEEE/AESS Radar Systems Panel where he is currently Chair of the Conferences Committee and the Nathanson Award Committee. He is an Associate Editor for *IEEE Transactions on Aerospace & Electronic Systems* and is on the Editorial Board for *IET Radar, Sonar & Navigation*. He was General Chair of the 2011 *IEEE Radar Conference* in Kansas City and is a member of the Program Committee for the *MSS Tri-Service Radar Symposium* series. He was Chair of the NATO SET-179 research task group on "Dynamic Waveform Diversity & Design" and a member of SET-182 on "Radar Spectrum Engineering & Management" and SET-227 on "Cognitive Radar".